Experimental Characterization of a Bearingless Rotating Field Axial-Force/Torque Motor

Walter Bauer[a], Paul Freudenthaler[b] and Wolfgang Amrhein[c]

Institute of Electrical Drives and Power Electronics, Johannes Kepler University, 4040 Linz, AUSTRIA, http://www.eal.jku.at
[a]walter.bauer@jku.at, [b]paul.freudenthaler@students.jku.at, [c]wolfgang.amrhein@jku.at

Abstract—The Bearingless Axial-Force/Torque Motor is an air-core coil motor, that can generate axial forces and drive torques concurrently using a common stator winding system. The radial suspension and the tilting stabilization of the bearingless drive is realized by passive repulsive permanent magnetic ring bearings. The end-windings of the concentric, non-overlapping stator coils create axial directed levitation forces, provided that a non-vanishing common-mode current component is present. In contrast to the existing alternating field motor topology, the proposed redesign features a rotating field motor structure for constant, rotor-angle independent drive torque generation. The current investigation concentrates on the verification of the drive parameters via simple and robust measurements. A presentation of the functional prototype concludes the article.

I. INTRODUCTION

In order to control the motion of a rigid rotor in three dimensional space, the dynamic behaviour of six degrees of freedom (DOFs) must be stabilized either passively by constructive measures or by active closed-loop position control.

A bearingless drive is a motor with an integrated magnetic bearing (levitation) functionality, which allows the reduction of the number of necessary (additional) bearings. The challenge in bearingless drive design is the stabilization of all the DOFs with the lowest possible constructive complexity.

In terms of control theory, the Bearingless Axial-Force/Torque Motors (AFTMs) are underactuated mechanical systems, which means, they possess fewer control inputs than DOFs. The passive dynamics[1] and the related passive DOFs must be asymptotically stable to ensure a proper overall drive functionality.

The passive permanent magnet ring bearing (PMB) unit is a basic component of the AFTM. A single repulsive PMB unit consists of two nested components, a stator ring and a rotor ring, both axially magnetized. The two interacting bearing rings provide stabilizing resilience forces in the radial directions, while destabilizing axial thrust and tilting torques are generated simultaneously. In order to eliminate those detrimental tilting torques, at least a second PMB unit, mounted on the same shaft axis with an axial displacement, is required. Thus, the lateral (radial) and the tilting directions (4 DOFs) of the AFTM are passively stabilized by the application of PMB technology avoiding any electrical energy consumption during drive operation.

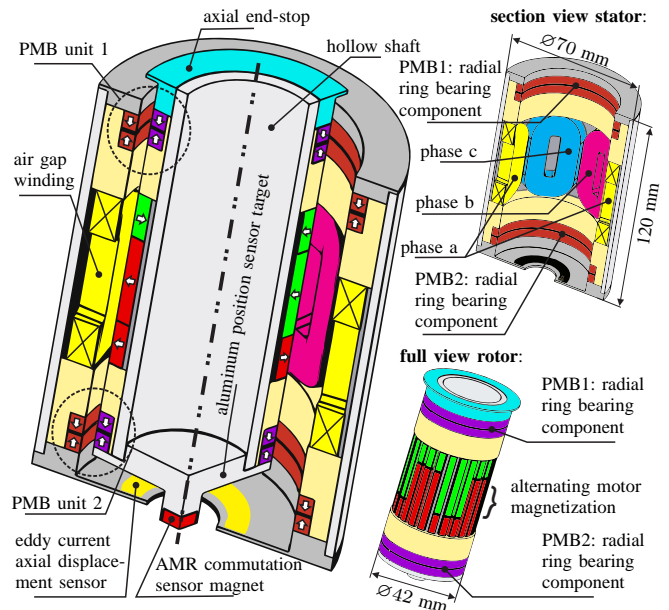[1]dynamical system behaviour, when not drawing energy from a supply

Figure 1. Schematic view of the Bearingless Rotating Field Axial-Force/Torque Motor in its operating position. The passive magnetic radial bearing (PMB) units are axially aligned. Inside rotor motor design with $p_r = 4$ segmented rotor pole pairs and $m = 6$ air-core coils.

The remaining two DOFs are the axial and angular rotor position. The axial position dynamics is unstable due to the introduced axial thrust caused by the PMB units and the gravitational forces.

The actuator part of the AFTM, basically a permanent magnet synchronous motor structure with an air gap stator winding, is responsible for active generation of axial compensation forces and drive torques. The air gap winding of an AFTM consists of m non-overlapping concentric air-core stator coils. The circumferential directed conductor sections of the bent stator coils are designated as the upper and lower end-windings. Together with a very specific magnetization pattern of the rotor magnet system, the energized coil ends can produce non-vanishing axial Lorentz forces. The impression of common-mode current components into the stator winding system result in rotor-angle independent active levitation forces.

The axial directed conductor sections of the stator coils provoke tangential Lorentz forces in combination with the cen-

trally arranged alternating pole motor magnetization pattern of the permanent magnet excitation system. The application of rotor-angle dependent, harmonic stator coil currents yield to constant drive torques.

The combined generation of active axial bearing forces and drive torques using just a single stator winding system with superimposed bearing and motor coil current components is a key feature of the AFTM.

A. State of the Art

The first prototype [1], [2] consists of $m = 4$ non-overlapping stator air-core coils and $p_r = 2$ rotor pole pairs. The outcome of this topology selection is an alternating field motor, showing a rather detrimental single-phase motor characteristics. In addition to the non-zero mean drive torque value, a drive torque component of equal amplitude, pulsating with the double synchronous rotor frequency, is present during motor operation.

On the other hand, the choice of $m = 4$ stator coils reliably avoids the appearance of rotor tilting during drive torque generation. The off-centric axial rotor forces, provoked by the energized coil ends, induce tilting torques referring to the rotors center of mass. Diagonally arranged stator coils, that share the same phase/coil current in amplitude and phase, mutually compensate their destabilizing tilting behaviour caused by the coil end-windings.

The bell-shaped rotor design of the Single-Phase AFTM offers various technical advantages over conventional drive concepts. Due to the both rotating back-irons, no eddy current and hysteresis losses can occur.

The extremely compact bearingless motor design is integrated into an electronic ventilator housing.

The high radial drive stiffness values of the PMBs facilitate the realization of a moderate drive tilting stiffness even with a small axial distance between the two PMB units.

Even though a single-phase motor characteristics is fully acceptable for the target application, the pulsating drive torque excitation raises questions about the dynamical behaviour of the rotor. Moreover, the geometric shape of the bell-rotor, which is in between a slice and slim, elongated spindle, is controversial in terms of its rotor dynamics.

The characteristic properties of a Bearingless AFTM, whether favorable or detrimental, strongly depend on the number of motor pole pairs p_r and the number of stator coils m. Certain combinations provoke disturbing radial forces during motor operation, others create drive torque ripple in case of common-mode stator current excitation. Furthermore, the circumferentially directed conductors (end-windings) of the coil system might promote the rotor tilting during drive torque generation in particular configurations.

The investigations in [3] have shown, that all rotating-field motor topology comes along with a rotor-angle dependent torque ripple during levitation force generation via common-mode currents. For the alternating-field motor toplogy, no torque ripple is present at all.
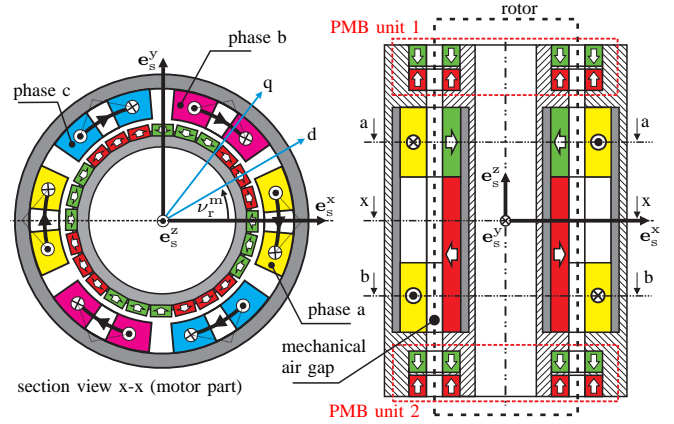

Figure 2. Full section view (2D) of the AFTM topology. Two diametrical opposing air core coils establish one electrical phase. (connection in series)
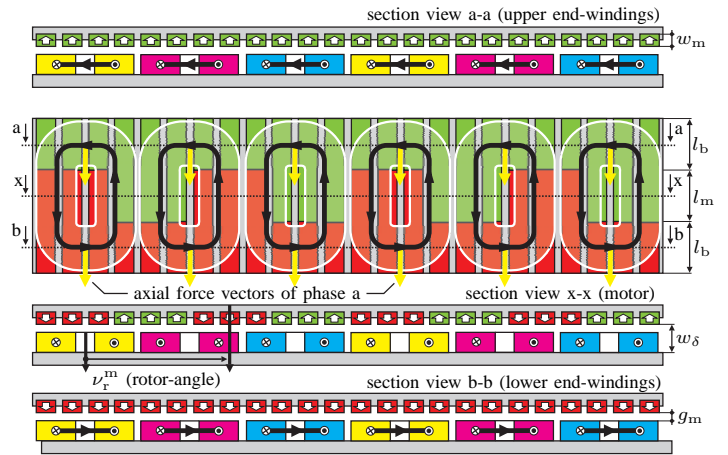

Figure 3. Developed view of the Rotating Field AFTM with segmented rotor magnet system.

B. Novel Actuator Topology

Referring to the first AFTM prototype, several modifcations have been undertaken at the current prototype design. The $m = 6$ non-overlapping air-core stator coils are grouped into three electrical phases. Together with $p_r = 4$ rotor pole-pairs realized by the segmented rotor permanent magnet system of Fig. 3, a rotor-angle independent, constant drive torque behaviour can be obtained. The expense for this favorable motor behaviour is the appearance of a small drive torque ripple during active levitation force generation via common-mode coil currents.

Moreover, the axial mounting distance of the radial PMB units has been augmented for higher resulting drive tilting stiffness values. While the chosen inside rotor drive topology benefits of one single mechanical air gap, the attainable drive speed is limited simultaneously due to its surface mounted rotor magnets.

C. Objectives of the Proposed Investigation

The current research is focused on the experimental verification of the system parameters for the new prototype drive using

simple and robust state of the art measurement procedures. A brief summary of the advanced mathematical description framework for Rotating-field AFTM topologies should highlight its distinctive features comparing to the existing Single-Phase formulation presented in [4]. Special emphasis is placed on the complete characterization of the Rotating Field AFTM for comprehensive dynamic system simulation and control system design. A comparison between measurement data and electromagnetic FEA calculations proves the validity of the numerical simulation methods and highlights the (small) discrepancies. Last but not least, a prototype presentation of the novel rotating field AFTM structure concludes the current article.

II. MODEL EQUATIONS

Given is the state-space description of the three electrical phases of a Rotating field synchronous machine with surface-mounted permanent magnets (SPM) in the stator reference frame, e.g. [5]. The three electrical winding phases do no have a common star point, i. e. they are galvanically isolated. The application of the Blondel-Park transformation

$$\mathbf{T} = \frac{2}{3} \begin{bmatrix} 1/2 & 1/2 & 1/2 \\ \cos\left(\nu_r^e\right) & \cos\left(\nu_r^e - \frac{2\pi}{3}\right) & \cos\left(\nu_r^e + \frac{2\pi}{3}\right) \\ -\sin\left(\nu_r^e\right) & -\sin\left(\nu_r^e - \frac{2\pi}{3}\right) & -\sin\left(\nu_r^e + \frac{2\pi}{3}\right) \end{bmatrix} \tag{1}$$

to the input phase voltage vector $\mathbf{u}$ and the phase current $\mathbf{i}$ state vector

$$\mathbf{u}^t = [u_a, u_b, u_c] \quad \text{and} \quad \mathbf{i}^t = [i_a, i_b, i_c] \tag{2}$$

using the input and state transformations

$$\mathbf{u}_e = \mathbf{T}\mathbf{u} \quad \text{and} \quad \mathbf{i}_e = \mathbf{T}\mathbf{i} \tag{3}$$

yields the affine, time-invariant dynamical system description

$$\mathbf{u}_e = \left(\mathbf{R} + \omega_s L_{ph} \mathbf{G}\right) \mathbf{i}_e + \mathbf{L} \frac{\mathrm{d}}{\mathrm{d}t} \mathbf{i}_e + \mathbf{u}_{p,e} \tag{4}$$

in the synchronous rotor reference frame $\{dq\}$. The synchronous, electrical stator frequency

$$\omega_s = p_r \Omega_z \tag{5}$$

is a function of the number of motor pole-pairs p_r and the mechanical rotor speed Ω_z. The rotation of the reference frame is covered by the permutation matrix

$$\mathbf{G} = \begin{bmatrix} 0 & 0 & 0 \\ 0 & 0 & -1 \\ 0 & 1 & 0 \end{bmatrix} \tag{6}$$

and ν_r^e denotes the electrical rotor angle. The transformed input voltages and currents in the rotor reference frame are

$$\mathbf{u}_e^t = [u_0, u_d, u_q] \quad \text{and} \quad \mathbf{i}_e^t = [i_0, i_d, i_q], \tag{7}$$

where the variables u_0 and i_0 designate the so called zero-sequence components. They are used for description of the common-mode voltage and current relations, which determine the dynamic behaviour of the active axial levitation forces of

the AFTM. Due to the non-overlapping air-core coil winding, no mutual inductance is present between the electrical phases. The magnetic coupling for adjacent air core coils is below 3% and therefore neglected for system modeling. The constant phase resistance $\mathbf{R}$ and phase inductance $\mathbf{L}$ matrices are

$$\mathbf{R} = \mathrm{diag}\{R_{ph}, R_{ph}, R_{ph}\} \quad \text{and} \tag{8}$$

$$\mathbf{L} = \mathrm{diag}\{L_{ph}, L_{ph}, L_{ph}\}, \tag{9}$$

where the phase inductance L_{ph} is determined by the leakage inductance only. As already mentioned, no magnetic coupling between the different winding phases is present. The transformed back-emf phase voltage vector of the SPM may be written as

$$\mathbf{u}_{p,e}\left(\Omega_z, \nu_r^e\right) = \Omega_z \begin{bmatrix} -k_{\Omega,3} \sin 3\nu_r^e \\ 0 \\ k_{\Omega,1} \end{bmatrix} \tag{10}$$

with the mechanical rotor speed $\Omega_z = \dot{\nu}_r^e / p_r$ and the speed constant of the harmonic order v

$$k_{\Omega,v} = p_r v \hat{\psi}_v. \tag{11}$$

$\hat{\psi}_v$ is the phase flux linkage amplitude of the electrical order number v. All higher harmonics above third order are neglected in (10). The mechanical output variables

$$\begin{bmatrix} t_r^z\left(\nu_r^e\right) \\ f_r^z \end{bmatrix} = \begin{bmatrix} -3k_{\Omega,3} \sin 3\nu_r^e & 0 & \frac{3}{2} k_{\Omega,1} \\ -k_f & 0 & 0 \end{bmatrix} \mathbf{i}_e \tag{12}$$

are linear functions of the transformed current vector $\mathbf{i}_e$. The active axial bearing forces f_r^z, realized by the coil end-windings, are controlled via the common-mode coil current component i_0, while zero-mean drive torque ripple is being generated simultaneously due to the presence of a third harmonic component in the back-emf phase voltage spectrum.

III. MEASUREMENTS

Due to the complex actuator geometry, numerical field calculations are indispensable for dimensioning of the drive components to fulfill the predefined design specifications. After prototype manufacturing, the device characterization using simple and robust measurement procedures is essential not only for design validation, but also for dynamical system simulation and control system design.

A. Radial Drive Stiffness

The total radial drive stiffness is composed of the stabilizing forces f_r^x of the passive PMB system and the destabilizing radial reluctance forces of the actuator part. The results of the strain gauge radial force measurements and the numerical calculations are depicted in Fig. 4. In case of a centered and undeflected rotor, no radial resilience forces occur. According to the measurement results, the stabilizing radial magnetic forces of the passive ring bearing units (PMBs) are reduced by the (relatively small) reluctance forces of the stator back-iron. The radial motor reluctance forces of the present prototype are
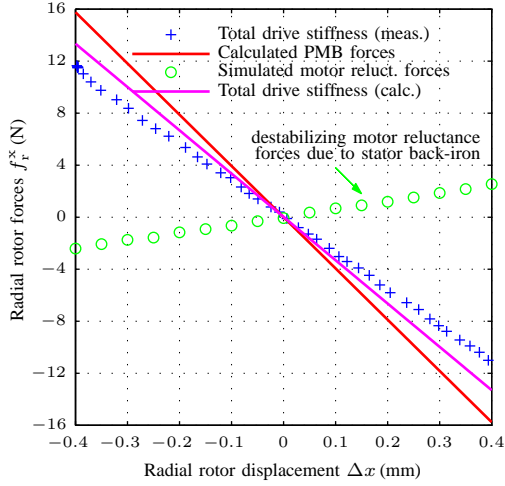
Figure 4. Radial drive stiffness measurements. Comparison between the semianalytic PMB radial stiffness calculations and the measured total radial drive forces. The radial force measurements include destabilizing radial reluctance forces of the actuator.

Figure 5. Spectral analysis of the back-emf voltage of phase a at $\Omega_z = 3480\,\text{rpm}$.

estimated using numerical 3D-fea simulations. The calculated destabilizing motor stiffness value is

$$s_{\text{mot}}^{\text{sim}} \approx -7\,\text{N/mm}. \tag{13}$$

The radial force characteristic of the ironless, passive magnetic ring bearings (PMB) is calculated by analytical methods. The inclusion of the numerical calculated motor stiffness value reduces the gap between measurement and calculation.

$$\frac{s_r^{\text{m}}}{s_r^{\text{sim}}} = \frac{30\,\text{N/mm}}{(39-7)\,\text{N/mm}} = 0.93 \tag{14}$$

B. Back-emf (No-load) Phase Voltage

A simple back-emf phase voltage measurement can provide valuable information about the torque capability and the drive torque ripple. The spectral analysis of the back-emf phase voltage at a constant rotor speed is illustrated in Fig. 5. The fundamental wave and third harmonic voltage amplitudes can be clearly identified. The flux linkage of phase a with the permanent magnet rotor excitation system

$$\psi_a\left(\nu_r^{\text{e}}\right) \approx \hat{\psi}_1 \cos \nu_r^{\text{e}} + \hat{\psi}_3 \cos 3\nu_r^{\text{e}} \tag{15}$$

is useful for the deduction of the back-emf voltage expression. The total time-derivative of (15) yields

$$\begin{aligned}
u_{\text{p,a}}\left(\nu_r^{\text{e}}\right) &= \frac{\mathrm{d}}{\mathrm{d}t}\psi_a = p_r\Omega_z\frac{\partial}{\partial\nu_r^{\text{e}}}\psi_a \\
&= -\Omega_z p_r\hat{\psi}_1 \sin \nu_r^{\text{e}} - \Omega_z p_r 3\hat{\psi}_3 \sin 3\nu_r^{\text{e}} \\
&= -\hat{u}_{\text{p,1}} \sin \nu_r^{\text{e}} - \hat{u}_{\text{p,3}} \sin 3\nu_r^{\text{e}}
\end{aligned} \tag{16}$$

with the back-emf voltage amplitude of the order v

$$\hat{u}_{\text{p,v}} = \Omega_z k_{\Omega,v} \tag{17}$$

as a linear function of the mechanical rotor speed Ω_z. A comparison of the measured fundamental wave and third harmonic wave back-emf phase voltage components, taken at
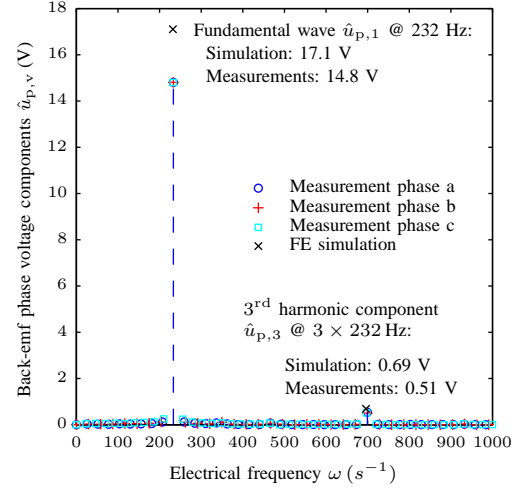
different mechanical speeds, is depicted in Fig. 6. The related speed constants are determined by calculation of the regression lines.

$$\frac{k_{\Omega,1}^{\text{m}}}{k_{\Omega,1}^{\text{sim}}} = \frac{4.242\,\text{mV/rpm}}{4.915\,\text{mV/rpm}} = 0.86 \tag{18}$$
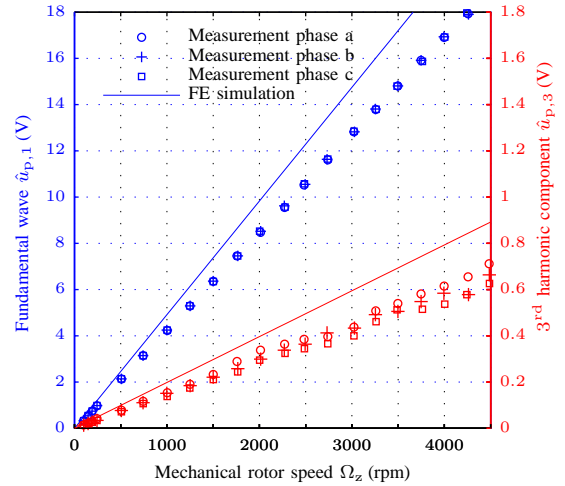

Figure 6. Comparison of the back-emf voltage measurements of three phases and determination of the back-emf speed constants $k_{\Omega,1}$ and $k_{\Omega,3}$.

C. Drive Torques

The second method for determination of the torque constant is the direct drive torque measurement via strain gauge torque sensor at constant phase current excitation.

1) Strain Gauge Measurement of Drive Torques: The drive torque expression of phase a at a constant phase current

$$\begin{aligned}
t_{\text{r,a}}^{\text{z}}\left(\nu_r^{\text{e}}\right) &= -i_a\left(k_{\Omega,1} \sin \nu_r^{\text{e}} + k_{\Omega,3} \sin 3\nu_r^{\text{e}}\right) \\
&= t_{\text{r,a1}}^{\text{z}}\left(\nu_r^{\text{e}}\right) + t_{\text{r,a3}}^{\text{z}}\left(\nu_r^{\text{e}}\right)
\end{aligned} \tag{19}$$

is composed of a fundamental wave and a third harmonic drive torque component. All other harmonics are neglected in (19), which is justified in view of the following measurement results. A spectral analysis of the single phase drive torque measurements for a constant phase current is depicted in Fig. 7.

$$\frac{k_{\Omega,1}^{m}}{k_{\Omega,1}^{sim}} = \frac{41\,mN.m/A}{46.5\,mNm/A} = 0.88 \tag{20}$$
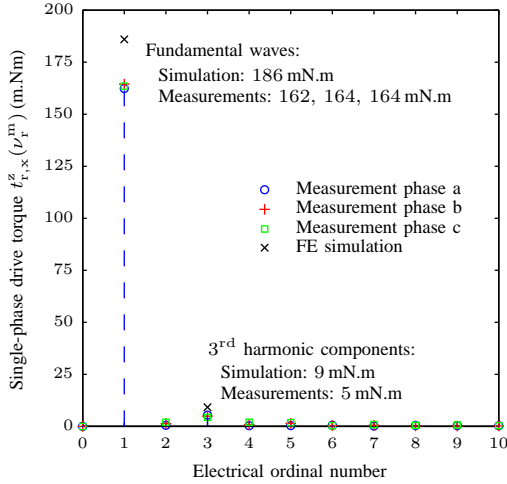

Figure 7. Single phase drive torque measurements via strain gauge torque sensor at $i_x = 4\,A$ with $x \in \{a, b, c\}$. The fundamental wave (dashed lines) and the third harmonic (plain lines) spectral decomposition of the measured torques have been added into the diagram.

2) Torque Ripple Measurement: For measuring the torque ripple provoked by the interacting third harmonic back-emf voltages and the common-mode stator currents, all electrical phases are excited with constant currents corresponding to

$$i_0 = i_a = i_b = i_c = 4\,A\,. \tag{21}$$

Two independent measurements of the drive torque ripple have been carried out. The results are depicted in Fig. 8 together with the superponed single phase torque measurements of Fig. 7. The drive torque ripple as a result of a zero-sequence current component i_0 in absence of a mean torque producing current component i_q is

$$t_r^z(\nu_r^e) = -3k_{\Omega,3}i_0\sin 3\nu_r^e\,, \tag{22}$$

referring to (12). The three phase-shifted fundamental harmonic torque components of the prototype machine do not compensate one another exactly, which can be seen easily in Fig. 7 . Due to a slight geometric unsymmetry of the stator winding geometry, the measured torque ripple in Fig. 8 contains a subharmonic component, that is not represented by (22).

D. Active Axial Bearing Forces

The measurement of the axial force as a function of the current i_0 has been effectuated using a strain gauge force/torque
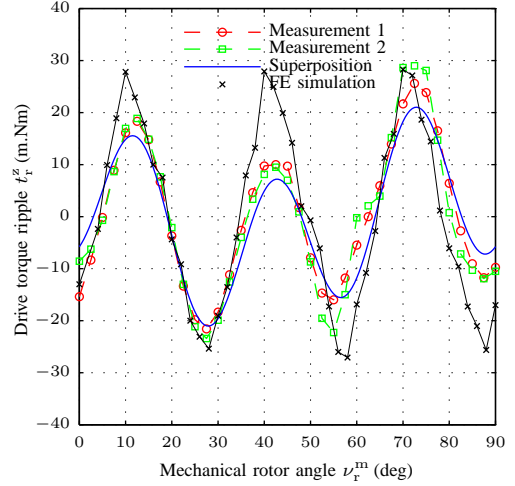

Figure 8. Direct measurement of the drive torque ripple at $i_0 = 4\,A$. Because of the small amplitudes, two independent measurements have been effectuated and plotted into a single diagram. The black line represents the superposition of the single phase torque measurements of Fig. 7.
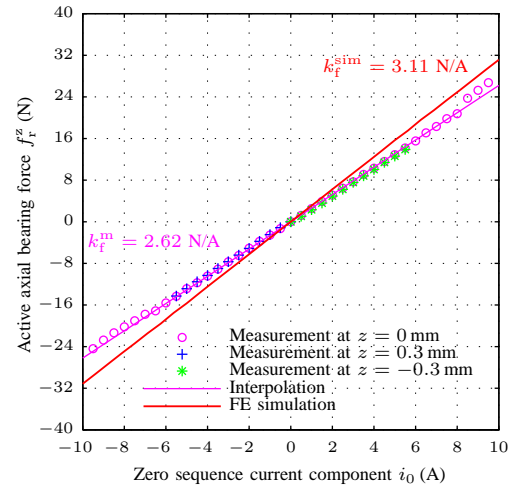

Figure 9. Determination of the axial force/current constant. Axial force measurements for two different axial deflections around the equilibrium position $z = 0$.

sensor. A comparison between measurement data and numerical force simulation is shown in Fig. 9. The discrepancy between the measured and simulated force/current constant

$$\frac{k_f^m}{k_f^{sim}} = \frac{2.62\,N/A}{3.11\,N/A} = 0.84 \tag{23}$$

is within the usual bandwidth of numerical 3d fea simulations.

IV. PROTOTYPE PRESENTATION

The stator air gap winding is depicted in Fig. 10 and the rotor of the Bearingless AFTM is shown in Fig. 11.

V. CONCLUSION

The dynamic behaviour of the novel polyphase AFTM is determined by a few system parameters only, which can be

Figure 10.   Experimental setup stator part. Air gap winding (expoxy resin bonded) with stator back iron.

Figure 11.   Experimental setup rotor.

determined either by time-consuming numerical 3d simulations or by more or less complicated and expensive device measurement methods. Both approaches yield comparable results.

REFERENCES

[1] W. Bauer and W. Amhrein, "Design and sizing relations for a novel bearingless motor concept," *ICEMS: International Conference on Electrical Machines and Systems, Beijing, China*, Aug. 20-23, 2011, DOI: 10.1109/ICEMS.2011.6073470.

[2] ——, "Electrical design and winding selection for a bearingless axial-force/torque motor," *SPEEDAM 2012: International Symposium on Power Electronics, Electrical Drives, Automation and Motion, Sorrento, Italy*, Sep. 19-20, 2013, DOI: 10.1109/SPEEDAM.2012.6264458.

[3] ——, "Design study of air-core coil winding topologies for bearingless axial-force/torque motors," *ISMB13: The 13th International Symposium on Magnetic Bearings, Arlington, VA, USA*, Aug. 6-9, 2012, http://www.magneticbearings.org.

[4] ——, "Performance analysis of a bearingless axial-force/torque motor," *9. GMM/ETG Symposium 2013: Innovative Small Drives and Micro-Motor Systems, Nuernberg, Germany*, Sep. 19-20, 2013, ISBN: 978-3-8007-3537-2.

[5] P. Vas, *Electric Machines and Drives - A space-vector theory approach*. Oxford University Press, 1992.

Table I
PROTOTYPE SPECIFICATIONS OF THE ROTATING-FIELD AXIAL-FORCE/TORQUE MOTOR.

Description	Symbol	Value	Unit
Number of stator coils	m	6	
Number of pole pairs	p_r	4	
Average air gap radius	R_δ	24	mm
Motor magnet height	l_m	10.5	mm
Active bearing magnet height	l_b	9.5	mm
Magnet width	w_m	2	mm
Electromagnetic air gap width	w_δ	6	mm
Mechanical air gap width	g_m	1	mm
Permanent magnet volume		6.4	cm^3
Copper volume		2.1	cm^3
Dc-link voltage	$U_{\text{dc-link}}$	48	V
Nb. of turns per coil	N_c	160	
Max. admissible drive speed	Ω_z	7900	rpm
Nb. of electrical phases		3	
Nb. of required half-bridges		6	
Max. output motor power	P_{mech}	122	W
Admissible RMS current density	S_t^{cu}	10	A.mm^{-2}
Short-time current density	S_f^{cu}	50	A.mm^{-2}
Admissible avg. drive torque	$\langle t_r^z \rangle$	147	mN.m
Active axial force at S_f^{cu}	$f_{s,50}^z$	21	N
Rotor mass	m_R	0.330	kg
Mass moment of inertia	J_z	1813	g.cm^2

Table II
COMPARISON OF MEASUREMENTS AND SIMULATION.

Description	Symbol	Calc.	Meas.	Unit
Radial PMB stiffness	s_r	39.4		N/mm
Tilting PMB stiffness	$s_{\varphi\varphi}$	25.2		N.m/rad
Coupling stiffness	$s_{\varphi r}$	-288		N
Radial motor stiffness	s_{mot}	-7		N/mm
Total radial drive stiffness	s_r	32	30	N/mm
Axial drive stiffness (unstable)	s_z	-78.8	-80.4	N/mm
Speed constant (fund. wave)	$k_{\Omega,1}$	4.915	4.242	mV/rpm
Torque constant	k_t	69.8	61.5	mN.m/A
Speed constant (3$^{\text{rd}}$ harmonic)	$k_{\Omega,3}$	198.2	137.7	uV/rpm
Axial force constant	k_f	3.1	2.6	N/A
Phase resistance	R_{ph}	2.78	2.72	V/A
Phase inductance	L_{ph}	2.36	2.16	mH